

Diffusion MRI microstructure models with *in vivo* human brain Connectom data: results from a multi-group comparison.

Uran Ferizi^{a,b,c,*}, Benoit Scherrer^{d,*}, Torben Schneider^{c,e,*}, Mohammad Alipoor^f, Odin Eufracio^g, Rutger H.J. Fick^h, Rachid Deriche^h, Markus Nilssonⁱ, Ana K. Loya-Olivas^g, Mariano Rivera^g, Dirk H.J. Poot^j, Alonso Ramirez-Manzanares^g, Jose L. Marroquin^g, Ariel Rokem^l, Christian Pötter^l, Robert F. Dougherty^l, Ken Sakaie^m, Claudia Wheeler-Kingshott^c, Simon K. Warfield^d, Thomas Witzelⁿ, Lawrence L. Waldⁿ, José G. Raya^a, Daniel C. Alexander^b

^aDepartment of Radiology, New York University School of Medicine, USA

^bCentre for Medical Image Computing, University College London, UK

^cDepartment of Neuroinflammation, Institute of Neurology, University College London, UK

^dComputational Radiology Laboratory, Boston Children's Hosp., Harvard University, USA

^ePhilips Healthcare, Guildford, Surrey, UK

^fChalmers University of Technology, Gothenburg, Sweden

^gCentro de Investigacion en Matematicas AC, Guanajuato, Mexico

^hAthena Project-Team, INRIA Sophia Antipolis - Méditerranée, France

ⁱLund University Bioimaging Center, Lund University, Sweden

^jErasmus Medical Center and Delft University of Technology, the Netherlands

^keScience Institute, University of Washington, USA

^lCenter for Cognitive and Neurobiological Imaging, Stanford University, USA

^mImaging Institute, The Cleveland Clinic, Cleveland, USA

ⁿA.A. Martinos Center for Biomedical Imaging, MGH, Harvard University, USA

Abstract

A large number of mathematical models have been proposed to describe the measured signal in diffusion-weighted (DW) magnetic resonance imaging (MRI) and infer properties about the white matter microstructure. However, a head-to-head comparison of DW-MRI models is critically missing in the field. To address this deficiency, we organized the “White Matter Modeling Challenge” during the International Symposium on Biomedical Imaging (ISBI) 2015 conference.

This competition aimed at identifying the DW-MRI models that best predict unseen DW data. *In vivo* DW-MRI data was acquired on the Connectom scanner at the A.A.Martinos Center (Massachusetts General Hospital) using gradients strength of up to 300 mT/m and a broad set of diffusion times. We focused on assessing the DW signal prediction in two regions: the genu in the corpus callosum, where the fibres are relatively straight and parallel, and the fornix, where the configuration of fibres is more complex. The challenge participants had access to three-quarters of the whole dataset, and their models were ranked on their ability to predict the remaining unseen quarter of data. In this paper we provide both an overview and a more in-depth description of each evaluated model, report the challenge results, and infer trends about the model characteristics that were associated with high model ranking.

This work provides a much needed benchmark for DW-MRI models. The acquired data and model details for signal prediction evaluation are provided online to encourage a larger scale assessment of diffusion models in the future.

Keywords: diffusion MRI, model selection, Connectom, brain microstructure, genu, fornix

*Joint first co-authors

Email address: uran.ferizi@med.nyu.edu (Uran Ferizi)

1. Introduction

Diffusion-weighted (DW) magnetic resonance imaging (MRI) provides a unique insight into the microstructure of living tissue and is increasingly used to study the microanatomy and development of normal functioning tissue as well as its pathology. Mathematical models for analysis and interpretation have been crucial for the clinical adoption of DW-MRI. Even though diffusion tensor imaging (DTI), which is based on a simple model of the DW-MRI signal, has shown promise in clinical applications (Assaf and Pasternak, 2008), e.g. Alzheimer’s dementia (Rose et al., 2000), Multiple Sclerosis (Werring et al., 2000) or brain tumors (Price et al., 2006), a much wider variety of DW-MRI models has been proposed to extract more information from the DW signal. Some models explicitly describe the underlying tissue microstructure in each voxel with a multicompartment approach (Stanisz et al., 1997; Panagiotaki et al., 2012; Nilsson et al., 2013). These models, also referred to as “models of the tissue” (Scherrer et al., 2015), include the ball-and-sticks model (Behrens et al., 2003, 2007), the Composite Hindered and Restricted Model of Diffusion (CHARMED) (Assaf and Basser, 2005), the Minimal Model of White Matter Diffusion (MMWMD) (Alexander et al., 2010; Dyrby et al., 2013), the ball-and-rackets model (Sotiropoulos et al., 2012), Neurite Orientation Dispersion and Density Imaging (NODDI) (Zhang et al., 2012) and DIAMOND (Scherrer et al., 2015). Other approaches focus on describing the DW signal attenuation without explicitly describing the underlying tissue composition that gives rise to the signal. These “models of the signal” (Scherrer et al., 2015) include Q-Ball imaging (Tuch, 2004; Descoteaux et al., 2007), the Cumulant Expansion (Liu et al., 2003; Kiselev, 2011), the Simple Harmonic Oscillator Based Reconstruction and Estimation (SHORE) (Ózarslan et al., 2008), the Mean Average Propagator (MAP) (Ózarslan et al., 2013) and Gaussian-Laguerre function-based q-space (Assemlal et al., 2009). Other approaches, in particular spherical deconvolution methods (Tournier et al., 2004; Jian et al., 2007), fall between these two extremes and include some features of the tissue, such as the distribution of fibre orientations, but often describe the signal from individual fibres without modelling the fibre composition explicitly.

Despite this explosion of DW-MRI models, competing methods are rarely tested and compared on a common data set and within a common evaluation framework. Panagiotaki et al. (2012) established a taxonomy of diffusion compartment models and compared 47 of them using data from the fixed corpus callosum of a rat acquired on a pre-clinical system. Ferizi et al. (2014) performed a similar experiment using data from a live human subject. Ferizi et al. (2013, 2015) explored a different class of models that aim to capture fiber dispersion. Rokem et al. (2015) compared two classes of models using cross-validation and test-retest accuracy. Nevertheless, the studies above are still limited only to certain classes of compartment models and don’t reflect the full variety within the field.

In other fields, publicly organized challenges have helped to establish a common ground for the evaluation of competing methods, e.g. registration of MRI brain images (Klein et al., 2009), diagnostic group classification for dementia using structural MRI (Bron et al., 2015), tissue segmentation on brain (Mendrik et al., 2015) and prostate (Litjens et al., 2014) tissue, on CT images for thoracic (Murphy et al., 2011), carotid (Hameeteman et al., 2011), and breathing airways (Lo et al.) tissue, fetal ultrasound images (Rueda et al., 2014), reconstruction methods using DW-MRI data acquired from a physical phantom (Ning et al.) or particle tracking (Chenouard et al., 2014) have been organized. In DW-MRI, public challenges have focused on recovering synthetic intra-voxel fibre configurations (Daducci et al., 2014) or evaluating tractography techniques (Pujol et al., 2015) and have been extremely successful at driving research and translation forward. Here we report on a different challenge within that research area that focusses on modeling the variation of DW-MRI signals at the voxel level. This assesses a key capability of diffusion MRI that previous challenges do not: that of recovering image-based biomarkers reflecting tissue microstructure.

The recent development of human MR systems with 300 mT/m gradients, in particular the Connectom scanner (Setsompop et al., 2013) is a major stepping stone towards DW-MRI data that is more sensitive to microstructural anatomy and organization of brain tissue. For example, Dyrby et al. (2013) illustrate the benefits of stronger gradients to map the axon diameters and other parameters in WM using fixed post-mortem tissue and a small-bore animal imaging system. The first experiments verifying those findings on live human subjects have now emerged from the Connectom scanner (McNab et al., 2013; Duval et al., 2014; Ferizi et al., 2015; Huang et al., 2015).

The rich data set from Ferizi et al. (2015), acquired on the Connectom system and sampling around five-thousand q -space points, offers the unique opportunity for the comparison of the many different types of models within a common framework, over a very wide range of the measurement space. Using this rich data set we organized the White Matter Modeling challenge, held during the ISBI conference in New York in 2015. The goal of the challenge was to identify the best model in two different tissue configurations that are common in the brain: 1) a white matter region of interest where fibers are relatively straight and parallel, specifically, the genu of the corpus callosum; and 2) a region in which the fiber configuration is more complex and contains crossing, specifically, the fornix. For both configurations, we provided a broad set of DW measurements that covers the set of b -values and diffusion times as widely as possible. Challenge participants had access to three-quarters of the whole data set; the participating models were evaluated on how well they predicted the remaining 'unseen' part of the data. As announced before the challenge, the final ranking was based exclusively on the performance on the genu data. However, we include in this paper results from both the genu and the fornix.

The paper is organized as follows. First, we describe in section 2 the experimental protocol, data post-processing and preparation of the training and testing data. We then describe the methods for ranking the models and succinctly present the various models involved in the competition. We report the challenge results in section 3 and discuss these results in section 4.

2. Material and Methods

2.1. The complete experiment protocol

One healthy volunteer was scanned over two 4h non-stop sessions. The imaged volume comprised twenty 4mm-thick whole-brain sagittal slices covering the corpus callosum left-right. The image size was 110 x 110 and the in-plane resolution 2 x 2 mm². Forty-five unique and evenly distributed diffusion directions (taken from <http://www.camino.org.uk>) were acquired for each shell, with both positive and negative polarities. We also included 10 interleaved $b=0$ measurements, leading to a total of 100 measurements per shell. Each shell had a unique combination of $\Delta = \{22, 40, 60, 80, 100, 120\}$ ms, $\delta = \{3, 8\}$ ms, and $|\mathbf{G}| = \{60, 100, 200, 300\}$ mT/m (see Table 1). The minimum possible echo time (TE) for each gradient duration and diffusion time combination was chosen to enhance SNR for shorter diffusion times. The SNR of $b = 0$ images was 35 at TE = 49 ms and 6 at TE = 152 ms. More details about the acquisition protocol can be found in Ferizi et al. (2015).

2.2. Post-processing

All post-processing was performed using FSL (Jenkinson et al., 2002). The DW images were corrected for eddy current distortions separately for δ and Δ combination using FSL's *Eddy* module (www.fmrib.ox.ac.uk/fsl/eddy) with default settings.

The images were then co-registered using FSL's *Fnirt* package. As the 48 shells were acquired across a wide range of echo times, over two days, we chose to proceed in two steps. First, within each quarter of the data set (different day, different δ) we registered all the $b=0$ images together. We then applied these transformations to their intermediary DW images. The second stage involved co-registering the four different quarters. To help the co-registration, especially between the two days' images that required some through-plane adjustment as well, we omitted areas of considerable eddy-current distortions by reducing the number of slices from 20 to 5 (two either side of the mid-sagittal plane) and reducing the in-plane image size to 75x80.

2.3. Training and testing data

The dataset was split into two parts: the training data set and the testing data set. The training dataset was fully available for the challenge participants. The testing dataset was retained by the organisers.

More precisely, we considered two ROIs, each containing 6 voxels (see Fig. 1). The first ROI was selected in the middle of the genu in the corpus callosum, where the fibres are mostly straight and coherent. The second ROI was selected in the fornix, where the fibre configuration is more complex.

The DW signal of the training dataset (36 shells, with acquisition parameters shown in black in Table 1) was provided together with the gradient scheme on the challenge website (<http://cmic.cs.ucl.ac.uk/wmmchallenge/>). This data was used by the participants to estimate their DW-MRI model. The signal attenuation in the testing dataset (12 shells, with acquisition parameters shown in red in Table 1) was kept unseen. Only the gradient scheme was provided; participants were then asked to predict the signal for the corresponding DW gradients. The challenge participants were free to use as much or as little of the training data provided to predict the signal of the test dataset for the six voxels in each ROI.

Figure 2 shows the DW signal attenuation for each shell in the genu data set, the arrows indicating which shells were left out for testing. It also shows a small number of outliers in some shells of the dataset. Specifically, we counted 10 of them among > 4800 measurements, most of them being in the $b = 300$ shell (bottom-left subplot in Figure 2). These may be attributed to momentary twitching of the subject during the long duration scan.

2.4. Models ranking

Models were evaluated and ranked based on their ability to accurately predict the unseen DW signal. Specifically, the metric used was the sum of square differences between the hidden signal and the predicted signal, corrected for Rician noise (Jones and Basser, 2004):

$$SSE = \sum_{i=1}^N \frac{(\tilde{S}_i - \sqrt{S_i^2 + \sigma^2})^2}{\sigma^2} \quad (1)$$

where N is the number of measurements, \tilde{S}_i is the i -th measured signal, S_i its prediction from the model, and σ is the noise standard deviation.

2.5. Competing models

We provide in Table 2 a summary of the key characteristics of the competing models. A more detailed description of each model is included in Appendix 2.5.

3. Results

Figure 3 shows the averaged prediction error in each ROI (top subplot: genu region; bottom subplot: fornix region) and the corresponding overall ranking of the participating models in the challenge. The first six models in the genu ranking performed similarly, each higher ranked model marginally improving on the prediction error. The prediction error clearly increased at a higher rate for the subsequent models. In the fornix dataset, the prediction error was higher than in the genu. For both datasets the first six models were the same, albeit permuted.

Most of the models performed similarly in terms of ranking in both genu and fornix cases, i.e. Nilsson (2nd in genu/1st in fornix), Scherrer (3rd/2nd) and Ferizi_2 (4th/4th). Others performed significantly better in one of the cases, with Ramirez-Manzanares (1st/6th) being the most notable.

Figure 4 shows the prediction error for each voxel independently, showing a similar group structure to the one observed in Figure 3. In the genu plot, the best performing models had high consistency of low prediction errors across all individual voxels. These were followed by the models with consistent larger prediction error in all voxels. Most of the lowest ranking models not only had largest prediction errors, they also showed large variations in prediction performance. For example, while the model of Loya-Olivas_2 was competitive in voxel 5, it ranked low due to large prediction errors in voxel 4 and voxel 6.

The results in the fornix were less homogeneous than in the genu, showing a lower consistency of prediction errors between voxels. Specifically, two voxels (3 and 4) showed substantially larger prediction errors and were likely responsible for much of the overall ranking.

Figure 5 details the prediction error for different ranges of b -values in the unseen dataset. It shows that the ranking between models was dominated by the signal prediction accuracy for b -values between 750 and 1400 s/mm^2 . The top-ranking models, nevertheless, were better at predicting the signal for higher b -value

images as well. The prediction performance of lower b -value images ($<750\text{s/mm}^2$) in the genu was less homogeneous across ranks. For example the models of Rokem and Sakaie outperformed most of the higher ranking models in this low b -value range. In the fornix, the prediction errors were generally larger than in the genu across all b -values for all models, except Rivera’s, which performed equally in both data sets. Prediction errors of the $b = 0$ images were also larger than in the genu, especially for the highly ranked models of Poot and Ferizi. The prediction errors in other b -value shells followed more closely the overall ranking of the models.

Finally, we report in Figure 6 and Figure 7 an illustration of the quality of fit of each model to 4 representative shells.

4. Discussion

4.1. Comments on the methods

The challenge was set out to identify the white matter models that best capture the DW signal. The fourteen challenge entries were a good representation of the many available models that are proposed in the literature. Table 2 synthesizes the main characteristics of the participating models, including the different strategies used for data fitting and pre-processing. Specifically, five models preprocessed the training data by clearing out outliers. These models were generally in the first half of the ranking. Four models used specific strategies to optimally predict the unseen signal (bootstrapping and cross-validation); two of them were ranked among the first (Ramirez-Manzanares; Nilsson). Four approaches chose to explicitly model the gradient pulse duration and separation δ and Δ , which in general was associated with a higher rank (Ramirez-Manzanares; Nilsson; Ferizi). Remarkably, models of the signal (Alipoor, Sakaie, Fick, Riviera) ranked on average lower than models of the tissues with our dataset, despite their theoretical ability to offer more flexibility in describing the raw signal. This may highlight the benefits of tissue models which, by incorporating *a priori* information about the expected signal, implicitly regularize the fit. In contrast, pure signal modelling approaches may be more prone to over-fit artifacts.

Only two models accounted for non-Gaussian noise in the signal, but this appeared to have little benefit on the ranking. Most participants used non-linear least-squares or maximum likelihood optimisation. Additional regularisation of the objective function (Eufrazio&Rivera/Lasso, Rokem/Elastic Net, Fick/Laplacian) appeared to have little benefit over regularized optimization.

4.2. Limitations and future directions

The large amount of DW data provided in the challenge supported the fitting of many parameters. However, we did not investigate the applicability of the models for more modest, clinically feasible protocols. Here we considered the most comprehensive DW scan acquired with the best possible hardware (the Connectom gradients), and assessed the intrinsic ability of DW models to capture the DW signal.

Assessing the prediction performance on unseen data as achieved in the challenge enables implicit penalisation of models which overfit the data. However, since all the missing shells were stray “between other shells (in terms of b -values, echo times, etc.), the quality of signal extrapolation was not assessed. This may be evaluated in future work by selecting “unseen” shells outside of the min-max range of experimental parameters.

The difference in error prediction between the best models was sometimes small; it was not entirely clear which characteristics were the main driver to the final performance (e.g., outlier rejection, noise modeling, etc.). We were, however, able to identify trends.

We did not take into account the computational demand of each model. Models that use bootstrapping might not be as effective on small datasets; on the other hand they may have a higher computational burden and may not be feasible for large datasets, e.g. whole brain coverage.

The dataset used in this challenge is specific to one subject who underwent a long duration acquisition, and thus questions remain about generalisability. The subsequent preprocessing of the data is also a factor to bear in mind: the registration of two 4h datasets, across such a broad range of echo times, poses its own challenges for certain non-homogenous regions in the brain, such as the fornix (as compared with, for

example, the relatively large genu). Therefore, because this long acquisition is not representative of any clinical *in vivo* protocol, many of the models will require more fine-tuning for clinical applications.

We focused here on comparing models based on their ability to predict unseen data. This enables comparison of the models' ability to capture the mechanism underlying the DW signal formation and provides useful information for the community. However, this does not capture the ability of estimated model parameters to provide useful information about the WM microstructure integrity such as the presence of axonal loss, demyelination or oedema in abnormal tissue.

The next step for the community should be to organise a challenge in which models are compared not only based on their ability to predict the signal, but also on their ability to accurately distinguish normal and abnormal tissue. This could be done by using synthetic substrates, either in-silico substrates (Hall and Alexander, 2009) or biomimetically designed phantoms (Hubbard et al., 2015), as well as DW-MR imaging of animal models of known tissue injuries and histological validation.

5. Acknowledgements

Research reported in this manuscript was supported by:

- EPSRC supported this work through grants EP/G007748, EP/L022680/1, EP/I027084/01, EP/M020533/1 and EP/N018702/1.
- U. Ferizi is also supported by the National Institute of Arthritis and Musculoskeletal and Skin Diseases (NIAMS) of the National Institute of Health (NIH) under award numbers R21AR066897 and RO1 AR067789.
- M. Nilsson is supported by the Swedish Strategic Research (SSF) Grant AM13- 0090
- B. Scherrer was supported in part by NIH R01 NS079788, R01 EB019483, R01 EB018988 and BCH TRP Pilot and BCH CTREC K-to-R Merit Award.

The content is solely the responsibility of the authors, and does not necessarily represent the official views of the funding bodies (EPSRC or NIH).

Lastly, we would like to thank ISBI 2015 challenge organisers, in particular, Stephen R. Aylward (Kitware Inc., USA) and Badri Roysam (University of Houston, USA).

6. Appendix: Competing models

6.1. Ramirez-Manzanares (CIMAT, Mexico): Empirical Diffusion-and-Direction Distributions (ED^3)

This work builds on the statistical modelling of the apparent diffusion coefficient (Yablonskiy et al., 2003), and tackles the modelling of axon fiber dispersion in single (Axer et al., 2001; Zhang et al., 2012) and multiple fibre bundle cases. The method empirically estimates (rather than impose) the distribution of tissue properties (axon radius, parallel diffusion, etc.), as well as the orientational distribution of the bundles. The general framework is as follows:

- estimation of mean principal diffusion directions (PDD) per axon bundle;
- selection of a dense set of orientationally-focused basis directions that capture the discrete non-parametric fiber dispersion;
- design of a dictionary of intra/extra cellular synthetic DW-signals which are precomputed along the basis directions (see the DBF method in Ramirez-Manzanares et al. (2007));
- computation of the size compartments per diffusion atom of the dictionary (model fitting).

The PDDs are estimated from the DT (single bundle case) and DBF (Ramirez-Manzanares et al., 2007) (complex structure cases). The 120 orientations closest to the PDDs are selected from a set of 1000, evenly distributed. The intra axonal signals S^i are precomputed from the model in Van Gelderen et al. (1994) for restricted diffusion within a cylinder with radius $R = 1, 2, \dots, 10 \mu\text{m}$ and parallel diffusion $d_{\parallel} = 1, 1.1, \dots, 2.1 \mu\text{m}^2/\text{ms}$. The extra axonal signals are generated as: S^e from *zeppelins* with combinations of parallel and radial diffusion, $d_{\parallel} = 1, 1.1, \dots, 2.5 \mu\text{m}^2/\text{ms}$ and $d_{\perp} = 2, 3, \dots, 8 \mu\text{m}^2/\text{ms}$, the isotropic diffusion compartment signals $S_k^{iso} = \exp^{-q\tau d_{iso}}$ for $d_{iso} = 2, 2.1, 2.2, \dots, 4 \mu\text{m}^2/\text{ms}$, and the *dot* signal that takes into account static proton density. The values of the dictionary-atoms above were tuned by cross validation. The size compartments $\beta \geq 0$ computed in the weighted non-negative LS formulation:

$$\left\| W \left(S - S_0^{TE} \left(\sum_{i=1}^{N_i} \beta_i^i S_i^i - \sum_{j=1}^{N_e} \beta_j^e S_j^e - \sum_{k=1}^{N_{iso}} \beta_k^{iso} S_k^{iso} + \beta_{dot} \right) \right) \right\|_2^2 \quad (2)$$

indicate the atoms that explain the signal, the W weights are proportional to SNR. Overfitting is reduced by a *bootstrap* procedure.

The atoms with coefficients $\beta > 0$ depict the empirical distributions, and their orientations indicate non-parametrical bundle-dispersion configurations (as fanning or radially symmetrical). The recovered distributions reveal, for instance, the presence of axon radius only among 1 and 4 μm . One should take into account, however, that since the heterogeneous intra/extra axonal T2 relaxation feature is not explicitly modelled, the method may compensate T2 variations by using, for instance, large isotropic d_{iso} coefficients to accurately fit the signal. For this reason, a direct interpretation of the fitted parameters may be misleading. The use of more specific models is a part of ongoing work.

6.2. Nilsson (Lund, Sweden) : Multi-compartment model outlier rejection and separate fitting of b_0 data

This multiple compartment model was developed specifically for the ISBI WM challenge and built up by a relaxation-weighted and time-dependent diffusion tensors according to

$$S = S_0 \sum_i w_i e^{-\mathbf{B}:\mathbf{D}_i} e^{-\text{TE}/\text{T2}_i} \left(1 - e^{-(\text{TR}-\text{TE}/2)/\text{T1}_i} \right) \quad (3)$$

where $\mathbf{B} = b\vec{n}^{\otimes 2}$ and $b = (\gamma\delta g)^2 t_d$. The diffusion time t_d was corrected for rise times (ξ) according to $t_d = \Delta - \delta/3 + \xi^3/30\delta^2 - \xi^2/6\delta$. Each component was also described by a weight (w_i) and relaxation times (T1_i and T2_i). The model featured three types of components, with either isotropic, hindered and restricted diffusion. Diffusion in the isotropic component was modeled by a single diffusion coefficient. The hindered and restricted components were modeled by cylinder-symmetric tensors described by axial and radial diffusivities together with the polar and azimuth angles. In the restricted component, the apparent diffusion coefficient of the radial component depended on δ and Δ , as well as on a cylinder radii, according to Vangelder et al. (1994).

Three modifications were performed to this very general model. First, to accommodate for potential bias in the b_0 images (which was the case for fornix data where deviations of up to 20σ was observed), the prediction for b_0 data was obtained from the median of all signals acquired with identical TE instead of from eq. 3. Second, anti-parallel acquisitions were rescaled by a free model parameter, in order to allow for potential gradient instabilities inducing differences between parallel and anti-parallel directions. Third, models were generated dynamically during fitting by randomly selecting up to four hindered components and up to three restricted components. One isotropic component was always included.

The model was first fitted to half of the diffusion-weighted data (randomly selected), after which outliers were rejected ($> 2.5\sigma$). Thereafter a second fit was performed. Both fit steps assumed Gaussian noise and utilized the 'lsqcurvefit' function in Matlab. The procedure was repeated 100 times for different randomly generated models.

To prepare for submission of the results, only the models that best predicted the hidden half of the data was selected, after which the median of the selected predictions were used for the final prediction.

6.3. Scherrer (Harvard, USA): Distribution of anisotropic microstructural environments in diffusion compartment imaging (DIAMOND)

DIAMOND models the set of tissue compartments in each voxel by a finite sum of unimodal continuous distributions of diffusion tensors. This corresponds to a hybrid tissue model that combines biophysical and statistical modeling. As described in (Scherrer et al., 2015), the DW signal S_k for a gradient vector \mathbf{g}_k and b-value b_k is modeled by: $S_k = S_0 \left[\sum_{j=0}^N f_j \left(1 + \frac{b_k \mathbf{g}_k^T \mathbf{D}_j^0 \mathbf{g}_k}{\kappa_j} \right)^{-\kappa_j} \right]$, where S_0 is the non-attenuated signal, N is the number of compartments and κ_j and \mathbf{D}_j^0 are respectively the concentration and the expectation of the j^{th} continuous tensor distribution. DIAMOND enables assessment of compartment-specific diffusion characteristics such as the compartment FA (cFA), the compartment RD (cRD) and the compartment MD (cMD). It also provides a novel measure of microstructural heterogeneity for each compartment.

The estimation of a continuous distribution of diffusion tensors requires DW data acquired with same timing parameters δ and Δ (Scherrer et al., 2015). Therefore, we fitted one DIAMOND model for each $\{\delta, \Delta\}$ group (*i.e.*, for each TE group), leading to 12 DIAMOND models. One shell was missing in each TE group; we predicted its signal using the corresponding DIAMOND model. The model estimation was achieved as follows. We first computed the mean and standard deviation of S_0 (μ_{S_0} and σ_{S_0}) within each TE group and discarded DW-signals whose intensity were larger than $\mu_{S_0} + 3\sigma_{S_0}$ (simple artefact correction). We then estimated DIAMOND parameters as described in Scherrer et al. (2015), considering Gaussian noise and cylindrical anisotropic compartments. For the genu we considered a model with one freely diffusing and one anisotropic compartment; for the fornix we considered a model with one freely diffusing compartment and two anisotropic compartments.

6.4. Ferizi_1 and Ferizi_2 (UCL, England)

This submission uses two three-compartment models, as described in previous studies (Ferizi et al., 2014, 2013). These models consist of: 1) either a Bingham distribution of sticks or a Cylinder for the intracellular compartment; 2) a diffusion tensor for the extracellular compartment; 3) an isotropic CSF compartment. The T_2 relaxation element is fitted beforehand, to the (variable echo time) $b=0$ measurements. The signal model is:

$$S = \tilde{S}_0 \left(f_i \exp\left(-\frac{TE}{T_2^i}\right) S_i + f_e \exp\left(-\frac{TE}{T_2^e}\right) S_e + f_c \exp\left(-\frac{TE}{T_2^c}\right) S_c \right) \quad (4)$$

where f_i , f_e and f_c are the weights of the intracellular, extracellular, and third normalised compartment signals S_{intra} , S_{extra} and S_c , respectively; the values of compartmental T_2 are indexed similarly; \tilde{S}_0 is the proton density signal (which is TE-independent, and obtained from fitting to the $b = 0$ signal). These models, as shown in the figure below, emerged from previous studies (see references below). Here, however, a single white matter T2 and separate compartmental diffusivities are additionally fitted.

There is a two-stage model fitting procedure. The first step estimates the T2 decay rate of tissue, separately in each voxel, by fitting a bi-exponential model to the $b=0$ intensity as a function of TE, in which one component is from tissue and the other from CSF. A preliminary analysis of voxels fully inside WM regions shows no significant departure from mono-exponential decay, equal T2 are then assumed within the intra and extracellular compartments. When fitting the bi-exponential model, the value of T2 in CSF is fixed to 1,000ms (a more precise value of CSF is unlikely to be estimated with this protocol). Thus, for each voxel, the volume fraction of CSF, the \tilde{S}_0 and the T2 of the tissue are estimated. These three estimates are then fixed for all the subsequent model fits. Then, each model is fitted using the Levenberg-Marquardt algorithm with an offset-Gaussian noise model.

6.5. Poot (Erasmus, the Netherlands)

This submission uses a three compartment model, with for each compartment a different complexity of the diffusion model and an individual T_2 value. This model was developed specifically for the ISBI WM challenge and is the result of iteratively visualizing different projections of the residuals and trying to infer the maximum complexity that the rich data supports.

The first compartment models isotropic diffusion and, through the initialization procedure, it captures the fast diffusion components. The second compartment is modelled by a second order (diffusion) tensor and models intermediate diffusion strengths. The third compartment is model-free as the ADC is estimated for each direction independently. Each compartment additionally has an individual T_2 value and signal intensity at $b = 0$, $TE = 0$ (which could easily be translated into volume fractions). Hence, the complete model of a voxel in image j is given by

$$S_j(\boldsymbol{\theta}) = \sum_{i=1}^3 A_i e^{-TE_j R_{2,i}} e^{-b_j ADC_{j,i}} = \sum_{i=1}^3 e^{\mathbf{M}_{i,j} \boldsymbol{\theta}} \quad (5)$$

where S_j is the predicted signal intensity of image j , A_i is the non-diffusion weighted signal intensity of compartment i at zero TE , TE is the echo time, R_2 is the reciprocal of the T_2 relaxation time of compartment i , $b = (\Delta - \delta/3)\delta^2|G|^2\gamma^2$, with $\gamma = 42.5781\text{MHz}/T$, $ADC_{j,1} = c$, $ADC_{j,2} = \mathbf{g}_j^T \mathbf{D} \mathbf{g}_j$, $ADC_{j,3} = \mathbf{d} \mathbf{h}_j^T$, where \mathbf{d} is a vector with the ADC value of each orientation group and \mathbf{h}_j is a vector that selects the orientation group to which image j belongs (90 groups in total). Note that \mathbf{h}_j has at most one nonzero element and that element has a value of one. As displayed in the right most part of Eq. (5), the model can be written as multiplication of matrices \mathbf{M}_i , containing all rows $\mathbf{M}_{i,j}$, with $\boldsymbol{\theta} = [\ln A_1, R_{2,1}, c, \ln A_2, R_{2,2}, D_{11}, D_{12}, D_{13}, D_{22}, D_{23}, D_{33}, \ln A_3, R_{2,3}, \mathbf{d}]^T$, which combines all 103 parameters into a single parameter vector. All parameters are simultaneously estimated from the provided 3311 measurements per voxel by a maximum likelihood estimator that assumes a Rician distribution of the measurements and simultaneously optimizes the noise level (Poot and Klein., 2015). The exact initialization and details of the optimization procedure are provided in the online supporting material. Finally, the signal intensities of the ?unseen? data are predicted by substituting the estimate into Eq. (5).

6.6. Alipoor (Chalmers, Sweden)

The DMRI signal is modeled as a fourth-order symmetric tensor as proposed by (Özarslan and Mareci, 2003). Let $\mathbf{g}_i = [x_i \ y_i \ z_i]$ and $\mathbf{a}_i = [z_i^4 \ 4y_i z_i^3 \ 6y_i^2 z_i^2 \ 4y_i^3 z_i \ y_i^4 \ 4x_i z_i^3 \ 12x_i y_i z_i^2 \ 12x_i y_i^2 z_i \ 4x_i y_i^3 \ 6x_i^2 z_i^2 \ 12x_i^2 y_i z_i \ 6x_i^2 y_i^2 \ 4x_i^3 z_i \ 4x_i^3 y_i \ x_i^4]^T$ be a gradient encoding direction and corresponding design vector, respectively. The diffusion signal is then described by

$$S(\mathbf{g}_i) = S_0 \exp\left(\frac{-TE}{T_2}\right) \exp(-b \mathbf{t}^T \mathbf{a}_i) \quad (6)$$

where $S(\mathbf{g}_i)$ is the measured signal when the diffusion sensitizing gradient is applied in the direction \mathbf{g}_i , S_0 is the observed signal in the absence of such a gradient, b is the diffusion weighting factor, and $\mathbf{t} \in \mathbb{R}^{15}$ contains the distinct entries of a fourth-order symmetric tensor. Note that $d(\mathbf{g}_i, \mathbf{t}) = d(\mathbf{g}_i)$ is used for simplification. Given measurements in $N > 15$ different directions, the least squares (LS) estimate of the diffusion tensor is $\hat{\mathbf{t}} = (\mathbf{G}^T \mathbf{G})^{-1} \mathbf{G}^T \mathbf{y}$ where where \mathbf{G} is an $N \times 15$ matrix defined $\mathbf{G} = [\mathbf{a}_1 \ \mathbf{a}_2 \ \dots \ \mathbf{a}_N]^T$ and $y_i = -b^{-1} \ln(S(\mathbf{g}_i)/S_0)$. We use the weighted LS tensor estimation method in (Alipoor et al., 2013) to mitigate the influence of outliers.

To estimate the diffusion signal for a given acquisition protocol with $TE = TE_x$, $b = b_x$ and $\delta = \delta_x$, the two non-diffusion weighted measurements with the closest TE s to TE_x (among measurements with $\delta = \delta_x$) are used to estimate T_2 and S_0 for each voxel. Then, data from the closet shell to b_x (among shells with $\delta = \delta_x$) are used to estimate the tensor describing the underlying structure.

6.7. Sakaie-Tatsuoka-Ghosh (Cleveland, USA): An Empirical Approach

As the extent of q-space in the dataset is unusually comprehensive, we chose a simple, generic approach to gain intuition. Visual inspection suggested use of a restricted and hindered component each with angular variation:

$$S_i = A_{TE_i} (f R_i + (1 - f) \exp(-b_i D_i)) \quad (7)$$

where S_i is the predicted signal for signal acquired with TE_i , b_i . A_{TE_i} is the median signal at a given TE with no diffusion weighting. Fit parameters are f , the volume fraction of R_i , the restricted component, and

D_i , the diffusivity. R_i and D_i are modeled as spherical harmonics with real, antipodal symmetry (Alexander et al., 2002) with maximum degree 4. The model has 31 fit parameters for each voxel. Data were fit using a nonlinear least squares algorithm (lsqcurvefit, MATLAB). Prior to the fit, data points with nonzero bvalue that had signal higher than the the median of the b=0 signal plus 1.4826 times the median absolute deviation were excluded. Shells with normalized median signal smaller than that of shells with lower bvalues were also excluded. Normalization was performed by dividing by the median of the b=0 signal with the same TE.

6.8. Rokem (Standford, USA): A restriction spectrum sparse fascicle model (RS-SFM)

The Sparse Fascicle Model, SFM (Rokem et al., 2015), is a member of the large family of models that account for the diffusion MRI signal in the white matter as a combination of signals due to compartments corresponding to different axonal fiber populations (fascicles), and other parts of the tissue. Model fitting proceeds in two steps. First, an isotropic component is fit. We model the effects of both the measurement echo time (TE), as well as the measurement b-value on the signal. These are fit as a $\log(TE)$ -dependent decay with a low order polynomial function, and a b-value-dependent multi-exponential decay (including also an offset to account for the Rician noise floor). The residuals from the isotropic component are then deconvolved with the perturbations in the signal due to a set of fascicle kernels each modeled as a radially symmetric ($\lambda_2 = \lambda_3$) diffusion tensor. The putative kernels are distributed in a dense sampling grid on the sphere. Furthermore, Restriction Spectrum Imaging (RSI (White et al., 2013)) is used to extend the model, by adding a range of fascicle kernels in each sampling point, with different axial and radial diffusivities, capturing diffusion at different scales. To restrict the number of anisotropic components (fascicles) in each voxel, and to prevent overfitting, the RS-SFM model employs the Elastic Net algorithm (EN (Zou and Hastie, 2005)), which applies a tunable combination of L1 and L2 regularization on the weights of the fascicle kernels. We used elements of the SFM implemented in the dipy software library (Garyfallidis et al., 2014) and the EN implemented in scikit-learn (Pedregosa et al., 2011). In addition, to account for differences in SNR, we implemented a weighted least-squares strategy whereby each signal’s contribution to the fit was weighted by its TE, as well as the gradient strength used. EN has two tuning parameters determining: 1) the ratio of L1-to-L2 regularization, and 2) the weight of the regularization relative to the least-squares fit to the signal. To find the proper values of these parameters, we employed k-fold cross-validation (Rokem et al., 2015), leaving out one shell of measurement in each iteration for cross-validation. We determined that the tuning parameters with the lowest LSE (Panagiotaki et al., 2012) provide an almost-even balance of L1 and L2 penalty with weak overall regularization. Because of the combination of a dense sampling grid (362 points distributed on the sphere), and multiple restriction kernels (45 per sampling point), the maximal number of parameters for the model is approximately 16,300, more than the number of data points. However, because regularization is employed, the effective number of parameters is much smaller, resulting in an active set of approximately 20 regressors (Zou et al., 2007). We have made code to fully reproduce our results available at <https://arokem.github.io/ISBI2015>.

6.9. Eufracio (CIMAT, Mexico): Diffusion Basis Functions for Multi-Shell Scheme

This model is based on the Diffusion Basis Functions (DBF) model (Ramirez-Manzanares et al., 2007), a discrete version of the Gaussian Mixture Model for the sphere: $\hat{s}_i = \sum_{j=1}^m \alpha_j \phi_{ij} + \epsilon$, with $\hat{s}_i = s_i/s_0$, $\phi_{ij} = \exp(-bq_i^T T_j q_i)$ and $T_j = (\chi_1 v_j v_j^T + \chi_2 I)$. The DBF model is reformulated by substituting ϕ_{ij} and T_j : $\hat{s}_i = \sum_{j=1}^m \alpha_j \exp(-b_i \chi_2 g_i^T g_i) \exp(-b_i \chi_1 (v_j^T g_i)^2) + \epsilon$. The first exponential can be defined as a scale factor that depends on the b-values, $\beta_i = \exp(-b_i \chi_2 q_i^T q_i)$. In this way, the β_i factors are associated with different b-values, so the new model includes the information of multi-shell schemes. The coefficients α and the shell scale factor β are computed by solving the optimisation problem:

$$\min_{\alpha, \beta_c} f(\alpha, \beta_c; \lambda_\alpha, \lambda_\beta) = \|B\tilde{\Phi}\alpha - S\|_2^2 + \lambda_\alpha \|\alpha\|_1 + \lambda_\beta \|\beta_c^0 - \beta_c\|_2^2 \quad \text{s.t. } \mathbf{1}^T \alpha = 1, \alpha \geq 0 \quad (8)$$

where $B = \text{diag}(\beta_c)$, $\beta_c = \frac{1}{\#C} \sum_{i \in C} \exp(-b_i \chi_2 (q_i^T q_i))$ and C is the set of indexes grouped by different b-values. The regularization term weighted by λ_α demands sparseness and the term weighted by

λ_β prevents an over-fitting. The problem in eq.(8) is solved in three steps. First, the active atoms are predicted ($\alpha_i > 0$) with $\tilde{\alpha} = \operatorname{argmin}_\alpha f(\alpha, \beta_c; \lambda_\alpha, \lambda_\beta)$. Second, the active atoms are corrected with $\alpha = \operatorname{argmin}_{\{\alpha_i\}: \tilde{\alpha}_i > 0} f(\alpha, \beta_c; 0, \lambda_\beta)$. Finally, the factors β_c are updated with $\beta_c = \operatorname{argmin}_{\beta_c} f(\alpha, \beta_c; \lambda_\alpha, \lambda_\beta)$. To solve each step, the active sets algorithm for quadratic programming is used.

To train the model for the WMM'15 data, eq.8 is solved for each voxel with the training data to find the optimal weights α_j and scale factors β_c that best reproduce the training data. For this challenge, the β_c factors are grouped by the 36 training shells and the method parameters are set by hand: $\lambda_\alpha = 0.5$, $\lambda_\beta = 0.02$, $\chi_1 = 9.5 \times 10^{-4}$ and $\chi_2 = 5 \times 10^{-5}$. To predict the unseen signal at each voxel, the reformulated model is used with the optimal weights α_j and the 12 scale factors for the unseen β_c are calculated by interpolation with the 36 optimal β_c of the training data.

6.10. Loya-Olivas (CIMAT, Mexico): Linear Acceleration of Sparse and Adaptive Diffusion Dictionary (LASADD)

LASADD is a multi-tensorial based technique to adapt dynamically the Diffusion Functions (DFs) dictionary to a DW-MRI signal (Loya-Olivas et al., 2015; Loya). The method changes size and orientation of relevant Diffusion Tensors (DTs). The optimisation algorithm uses a special DT expression and assumptions to reduce the computational cost.

The one-compartment version (LASADD-1C) is based on DBF multi-tensor model (Ramirez-Manzanares et al., 2007): $s_i^* = \sum_{j=1}^n \alpha_j \phi_{i,j}$ where $s_i^* = \frac{s_i}{s_{0i}}$, $\phi_{i,j} = \exp(-b_i \mathbf{g}_i^T \mathbf{T}_j \mathbf{g}_i)$, $\alpha_j > 0$, and $\sum_{j=1}^n \alpha_j = 1$. LASSAD express the DT as

$$\mathbf{T}_j = \chi_{1j} \mathbf{v}_j \mathbf{v}_j^T + \chi_{2j} \mathbf{I}, \quad (9)$$

where $\chi_{\{1,2\}j}$ are scalars associated to the eigenvalues, \mathbf{v}_j is the Principal Diffusion Direction (PDD), and \mathbf{I} is the identity matrix. The algorithm iterates three steps, like Aranda et al. (2015a,b): Predict, Correct, and Generate, until convergence. Prediction selects the relevant DFs using LASSO to regulate the number to choose. Correction adjusts volume fraction, size, and orientation of the DTs. Taking advantage of DT expression and Taylor first order series approximation of the exponential, the optimisations are reduced to bounded Least Squares problems which are solved by a Projected Gauss-Seidel scheme. Generation controls the overestimation of fibers by adding to the basis the resulted DTs of combining two and three DFs for the new iteration.

An extra refinement to the computed results, named LASADD-3C, splits each detected DF into three compartments (Sherbondy et al., 2010): intracellular (IC), extracellular (EC) and CSF. The multi-tensor model is $s_i^* = \sum_{j=1}^n \alpha_j^{IC} \psi_{i,j} + \sum_{j=1}^n \alpha_j^{EC} \theta_{i,j} + \alpha^{CSF} \omega_i$ with $\sum_{j=1}^n (\alpha_j^{IC} + \alpha_j^{EC}) + \alpha^{CSF} = 1$. The $\psi_{i,j}$ models the directional IC compartment diffusion for each fiber bundle using $\mathbf{T}_j^{IC} = \chi_{0j} \mathbf{v}_j \mathbf{v}_j^T$. The EC compartment with hindered diffusion uses the representation (9) for $\theta_{i,j}$. The isotropic diffusion ω_i uses $\mathbf{T}^{CSF} = \chi_3 \mathbf{I}$. This stage keeps fixed the PDDs and only adjust the α 's and χ 's of the three compartments.

The parameters of the models were estimated using the training data set: the b values using the equation by Stejskal and Tanner (1965) and the S_0 values as the median of the gradient-free signals with equal echo time per voxel. The initial basis comprises 33 PDDs distributed in the unitary sphere. The bounds $\chi_{\{0,1\}} \in [1, 39] \times 10^{-4}$ and $\chi_{\{2,3\}} \in [1, 9] \times 10^{-4} \text{mm}^2/\text{s}$ and the LASSO regularisation parameter (equals 1.7) were tuned by hand such that provides the minimum error. The best multi-tensorial model for both algorithms was used for each voxel to predict the corresponding unseen data.

6.11. Fick (INRIA, France): A Spatio-Temporal Functional Basis to Represent the Diffusion MRI Signal

We use our recently proposed spatio-temporal (3D+t) functional basis (Fick et al., 2015) to simultaneously represent the diffusion MRI signal over three-dimensional wave vector \mathbf{q} and diffusion time τ . Based on Callaghan's theoretical model of spatio-temporal diffusion in pores (Callaghan, 1995), our basis represents the 3D+t diffusion signal attenuation $E(\mathbf{q}, \tau)$ as product of a spatial and temporal functional basis as

$$E(\mathbf{q}, \tau) = \sum_{N=0}^{N_{\max}} \sum_{\{jlm\}} \sum_{o=0}^{O_{\max}} c_{\{jlm\}o} S_{jlm}(\mathbf{q}, u_s) T_o(\tau, u_t) \quad (10)$$

where T_o is our temporal basis with basis order o and S_{jlm} is the spatial isotropic MAP-MRI basis (Özarslan et al., 2013) with radial and angular basis orders j, l and m . Here N_{\max} and O_{\max} are the maximum spatial and temporal order of the bases, which can be chosen independently. We formulate the bases themselves as

$$\begin{aligned} S_{jlm}(\mathbf{q}, u_s) &= \sqrt{4\pi} i^{-l} (2\pi^2 u_s^2 q^2)^{l/2} e^{-2\pi^2 u_s^2 q^2} L_{j-1}^{l+1/2}(4\pi^2 u_s^2 q^2) Y_l^m(\mathbf{u}) \\ T_o(\tau, u_t) &= \exp(-u_t \tau / 2) L_o(u_t \tau) \end{aligned} \quad (11)$$

with u_s and u_t the spatial and temporal scaling functions, Y_l^m the spherical harmonics and L_o a Laguerre polynomial. We calculate the spatial scaling u_s by fitting an isotropic tensor to the TE-normalized signal attenuation $E(\mathbf{q}, \cdot)$ for all \mathbf{q} . Similarly, we compute u_t by fitting an exponential $e^{-u_t \tau / 2}$ to $E(\cdot, \tau)$ for all τ . We fit our basis using Laplacian-regularized least squares in the following steps: We first denote $\Xi_i(\mathbf{q}, \tau, u_s, u_t) = S_{jlm(i)}(\mathbf{q}, u_s) T_{o(i)}(\tau, u_t)$ with $i \in \{1 \dots N_{\text{coef}}\}$ with N_{coef} the number of fitted coefficients. We then construct a design matrix $\mathbf{Q} \in \mathbb{R}^{N_{\text{data}} \times N_{\text{coef}}}$ with $\mathbf{Q}_{ik} = S_{N_i}(\mathbf{A}, \mathbf{q}_k) T_{o_i}(\tau_k, u_t)$. The signal is then fitted as $\mathbf{c} = \text{argmin}_{\mathbf{c}} \|\mathbf{y} - \mathbf{Q}\mathbf{c}\|^2 + \lambda U(\mathbf{c})$ with \mathbf{y} the measured signal, \mathbf{c} the fitted coefficients and λ the weight for our analytic Laplacian regularization $U(\mathbf{c})$. We used generalized cross-validation (Craven and Wahba, 1978) to find the optimal regularization weighting λ in every voxel. In our submitted results, we used a spatial order of 8 and a temporal order of 4, resulting in 475 fitted coefficients.

6.12. Rivera: Baseline Method: Robust Regression

We regard this very simplistic model as a baseline for other model-based methods. It assumes as little information as possible from the diffusion signal. The vector of independent variables is $x_i = [g_i, |G|_i, \Delta_i, \delta_i, TE_i, b_i]$, containing the gradient strength g , the echo time TE and the b-value b . Given signal s_i , we then estimate the parameters of the linear regression model:

$$s = X\theta + \epsilon \quad (12)$$

where $\theta \in \mathbb{R}^{23}$ is the unknown vector of coefficients, ϵ is the residual error and

$$X = [x, x|^2, \Delta \delta, \Delta TE, \Delta b, \delta TE, \delta b, TE b, 1]$$

is the *matrix design* ($x|^2$ is obtained from squaring each element of the matrix x). To account for outliers we estimate θ with a weighted (robust) least squares approach using the Lasso Regularization:

$$\theta^{t+1} = \text{argmin}_{\theta} \|W^t(X\theta - y)\|_2^2 + \lambda \|\theta\|_1 \quad (13)$$

where W^0 is the identity matrix and each subsequent W computed via:

$$W^{t+1} = \text{diag}(v_i^{t+1} w_i^{t+1}) \quad (14)$$

with outlier weighting in $\omega_i^{t+1} = \kappa^2 / (\kappa^2 + (y_i - X\theta_i^{t+1})^2)$ though κ , an arbitrary parameter that controls the outlier sensitivity. The protocol weight

$$v_i^{t+1} = \text{mean}_{j \in \Omega_i} \{w_j^{t+1}\} \text{ and } \Omega_i = \{j : TE_j = TE_i, |G_j| = |G_i|\} \quad (15)$$

computes a confidence factor for the complete protocol.

The equations (13) and (14) are iterated three times. The final estimated signal is computed using (12), using the protocol of the unseen signal.

References

References

Alexander, D., Barker, G., Arridge, S., 2002. Detection and modeling of non-Gaussian apparent diffusion coefficient profiles in human brain data. *Magnetic Resonance in Medicine* 48, 331–340.

- Alexander, D.C., Hubbard, P.L., Hall, M.G., Moore, E.A., Ptito, M., Parker, G.J., Dyrby, T.B., 2010. Orientationally invariant indices of axon diameter and density from diffusion MRI. *NeuroImage* 52, 1374–1389.
- Alipoor, M., Gu, I.Y., Mehnert, A.J., Lilja, Y., Nilsson, D., 2013. On high order tensor-based diffusivity profile estimation, in: *Engineering in Medicine and Biology Society (EMBC), 2013 35th Annual International Conference of the IEEE*, pp. 93–96.
- Aranda, R., Ramirez-Manzanares, A., Rivera, M., 2015a. Recovering Detailed intra-voxel White Matter Structure by using an Adaptive Diffusion Dictionary, Presented in the ISMRM 23rd Annual Meeting and Exhibition, Toronto, Ontario, Canada.
- Aranda, R., Ramirez-Manzanares, A., Rivera, M., 2015b. Sparse and Adaptive Diffusion Dictionary (SADD) for recovering intra-voxel white matter structure. *Medical Image Analysis* 26, 243–255.
- Assaf, Y., Basser, P.J., 2005. Composite hindered and restricted model of diffusion (CHARMED) MR imaging of the human brain. *Neuroimage* 27, 48–58.
- Assaf, Y., Pasternak, O., 2008. Diffusion tensor imaging (DTI)-based white matter mapping in brain research: a review. *Journal of molecular neuroscience : MN* 34, 51–61.
- Asselmlal, H.E., Tschumperlé, D., Brun, L., 2009. Efficient and robust computation of pdf features from diffusion MR signal. *Medical image analysis* 13, 715–729.
- Axer, H., Axer, M., Krings, T., Graf Diedrich v. Keyserlingk, D., 2001. Quantitative estimation of 3-d fiber course in gross histological sections of the human brain using polarized light. *Journal of Neuroscience Methods* 105, 121–131.
- Behrens, T., Berg, H.J., Jbabdi, S., Rushworth, M., Woolrich, M., 2007. Probabilistic diffusion tractography with multiple fibre orientations: What can we gain? *NeuroImage* 34, 144–155.
- Behrens, T., Woolrich, M., Jenkinson, M., Johansen-Berg, H., Nunes, R., Clare, S., Matthews, P., Brady, J., Smith, S., 2003. Characterization and propagation of uncertainty in diffusion-weighted MR imaging. *Magnetic resonance in medicine* 50, 1077–1088.
- Bron, E.E., Smits, M., van der Flier, W.M., Vrenken, H., Barkhof, F., Scheltens, P., Papma, J.M., Steketee, R.M., Orellana, C.M., Meijboom, R., et al., 2015. Standardized evaluation of algorithms for computer-aided diagnosis of dementia based on structural MRI: The caddementia challenge. *NeuroImage* 111, 562–579.
- Callaghan, P.T., 1995. Pulsed-gradient spin-echo nmr for planar, cylindrical, and spherical pores under conditions of wall relaxation. *Journal of Magnetic Resonance, Series A* 113, 53–59.
- Chenouard, N., Smal, I., et al., 2014. Objective comparison of particle tracking methods. *Nature methods* 11, 281–289.
- Craven, P., Wahba, G., 1978. Smoothing noisy data with spline functions. *Numerische Mathematik* 31, 377–403.
- Daducci, A., Canales-Rodriguez, E.J., Descoteaux, M., Garyfallidis, E., Gur, Y., Lin, Y.C., Mani, M., Merlet, S., Paquette, M., Ramirez-Manzanares, A., et al., 2014. Quantitative comparison of reconstruction methods for intra-voxel fiber recovery from diffusion MRI. *Medical Imaging, IEEE Transactions on* 33, 384–399.
- Descoteaux, M., Angelino, E., Fitzgibbons, S., Deriche, R., 2007. Regularized, fast, and robust analytical Q-ball imaging. *Magnetic Resonance in Medicine* 58, 497–510.
- Duval, T., McNab, J., Setsompop, K., Witzel, T., Schneider, T., Susie Yi, H., Keil, B., Klawitter, E., Wald, L., Cohen-Adad, J., 2014. In vivo estimation of axon diameter in the human spinal cord using 300 mT/m gradients., in: *Joint Annual Meeting ISMRM-ESMRMB 2014*, Milan, Italy.
- Dyrby, T.B., Hall, M.G., Ptito, M., Alexander, D., et al., 2013. Contrast and stability of the axon diameter index from microstructure imaging with diffusion MRI. *Magnetic Resonance in Medicine* 70, 711–721.
- Ferizi, U., Schneider, T., Panagiotaki, E., Nedjati-Gilani, G., Zhang, H., Wheeler-Kingshott, C.A., Alexander, D.C., 2014. A ranking of diffusion MRI compartment models with in vivo human brain data. *Magnetic Resonance in Medicine* 72, 1785–1792.
- Ferizi, U., Schneider, T., Tariq, M., Wheeler-Kingshott, C., Zhang, H., Alexander, D., 2013. The importance of being dispersed: A ranking of diffusion MRI models for fibre dispersion using in vivo human brain data, in: Mori, K., Sakuma, I., Sato, Y., Barillot, C., Navab, N. (Eds.), *Medical Image Computing and Computer-Assisted Intervention MICCAI 2013*. Springer Berlin Heidelberg. volume 8149 of *Lecture Notes in Computer Science*, pp. 74–81.
- Ferizi, U., Schneider, T., Zhang, H., Wheeler-Kingshott, C.A., Alexander, D.C., 2015. White matter compartment models for in vivo diffusion MRI at 300 mt/m. *NeuroImage* .
- Fick, R., Wassermann, D., Pizzolato, M., Deriche, R., 2015. A unifying framework for spatial and temporal diffusion in diffusion MRI.
- Garyfallidis, E., Brett, M., Amirbekian, B., Rokem, A., van der Walt, S., Descoteaux, M., Nimmo-Smith, I., Dipy Contributors, 2014. Dipy, a library for the analysis of diffusion MRI data. *Front. Neuroinform.* 8, 8.
- Hall, M.G., Alexander, D.C., 2009. Convergence and parameter choice for monte-carlo simulations of diffusion MRI. *Medical Imaging, IEEE Transactions on* 28, 1354–1364.
- Hameeteman, K., Zuluaga, M.A., et al., 2011. Evaluation framework for carotid bifurcation lumen segmentation and stenosis grading. *Medical image analysis* 15, 477–488.
- Huang, S.Y., Nummenmaa, A., Witzel, T., Duval, T., Cohen-Adad, J., Wald, L.L., McNab, J.A., 2015. The impact of gradient strength on in vivo diffusion MRI estimates of axon diameter. *NeuroImage* 106, 464–472.
- Hubbard, P.L., Zhou, F.L., Eichhorn, S.J., Parker, G.J., 2015. Biomimetic phantom for the validation of diffusion magnetic resonance imaging. *Magnetic Resonance in Medicine* 73, 299–305.
- Jenkinson, M., Bannister, P., Brady, M., Smith, S., 2002. Improved optimization for the robust and accurate linear registration and motion correction of brain images. *NeuroImage* 17, 825–841.
- Jian, B., Vemuri, B.C., Özarslan, E., Carney, P.R., Mareci, T.H., 2007. A novel tensor distribution model for the diffusion-weighted MR signal. *NeuroImage* 37, 164–176.
- Jones, D.K., Basser, P.J., 2004. squashing peanuts and smashing pumpkins: How noise distorts diffusion-weighted MR data. *Magnetic Resonance in Medicine* 52, 979–993.

- Kiselev, V.G., 2011. The cumulant expansion: an overarching mathematical framework for understanding diffusion NMR. *Diffusion MRI: Theory, Methods, and Applications*, 152–168.
- Klein, A., Andersson, J., Ardekani, B.A., Ashburner, J., Avants, B., Chiang, M.C., Christensen, G.E., Collins, D.L., Gee, J., Hellier, P., et al., 2009. Evaluation of 14 nonlinear deformation algorithms applied to human brain MRI registration. *Neuroimage* 46, 786–802.
- Litjens, G., Toth, R., et al, 2014. Evaluation of prostate segmentation algorithms for MRI: the promise12 challenge. *Medical image analysis* 18, 359–373.
- Liu, C., Bammer, R., Moseley, M.E., 2003. Generalized diffusion tensor imaging (GDTI): A method for characterizing and imaging diffusion anisotropy caused by non-gaussian diffusion. *Israel Journal of Chemistry* 43, 145–154.
- Lo, P., van Ginneken, B., Reinhardt, J.M., et al, t., .
- Loya, A.K., . Algoritmos para Solución de Modelos No Lineales en DW-MRI, school = Centro de Investigación en Matemáticas, A.C., year = 2015, month = 2, . Master’s thesis.
- Loya-Olivas, A., Aranda, R., Rivera, M., 2015. LASADD: Linear Acceleration Method for Adapting Diffusion Dictionaries, Presented in the ISMRM 23rd Annual Meeting and Exhibition, Toronto, Ontario, Canada.
- McNab, J.A., Edlow, B.L., Witzel, T., Huang, S.Y., Bhat, H., Heberlein, K., Feiweier, T., Liu, K., Keil, B., Cohen-Adad, J., et al., 2013. The human connectome project and beyond: Initial applications of 300mT/m gradients. *NeuroImage* 80, 234–245.
- Mendrik, A., Vincken, K., Kuijf, H., et al, 2015. MRBrainS challenge: Online evaluation framework for brain image segmentation in 3t MRI scans. *Computational Intelligence and Neuroscience* .
- Murphy, K., Van Ginneken, B., Reinhardt, J.M., Kabus, S., Ding, K., Deng, X., Cao, K., Du, K., Christensen, G.E., Garcia, V., et al., 2011. Evaluation of registration methods on thoracic CT: the EMPIRE10 challenge. *Medical Imaging, IEEE Transactions on* 30, 1901–1920.
- Nilsson, M., van Westen, D., Ståhlberg, F., Sundgren, P.C., Lätt, J., 2013. The role of tissue microstructure and water exchange in biophysical modelling of diffusion in white matter. *Magnetic Resonance Materials in Physics, Biology and Medicine* 26, 345–370.
- Ning, L., Laun, F., Gur, Y., DiBella, E.V., Deslauriers-Gauthier, S., Megherbi, T., Ghosh, A., Zucchelli, M., Menegaz, G., Fick, R., et al., . Sparse reconstruction challenge for diffusion MRI: Validation on a physical phantom to determine which acquisition scheme and analysis method to use? *Medical Image Analysis* .
- Özarslan, E., Koay, C., Basser, P., 2008. Simple harmonic oscillator based estimation and reconstruction for one-dimensional q-space MR, in: *Proc. Intl. Soc. Mag. Reson. Med*, p. 35.
- Özarslan, E., Koay, C.G., Shepherd, T.M., Komlosh, M.E., İrfanoğlu, M.O., Pierpaoli, C., Basser, P.J., 2013. Mean apparent propagator (MAP) MRI: A novel diffusion imaging method for mapping tissue microstructure. *NeuroImage* 78, 16–32.
- Özarslan, E., Mareci, T.H., 2003. Generalized diffusion tensor imaging and analytical relationships between diffusion tensor imaging and high angular resolution diffusion imaging. *Magn Reson Med* 50, 955–965.
- Panagiotaki, E., Schneider, T., Siow, B., Hall, M.G., Lythgoe, M.F., Alexander, D.C., 2012. Compartment models of the diffusion MR signal in brain white matter: a taxonomy and comparison. *NeuroImage* 59, 2241–2254.
- Pedregosa, F., Varoquaux, G., Gramfort, A., Michel, V., Thirion, B., Grisel, O., Blondel, M., Prettenhofer, P., Weiss, R., Dubourg, V., et al., 2011. Scikit-learn: Machine learning in python. *The Journal of Machine Learning Research* 12, 2825–2830.
- Poot, D., Klein, S., 2015. Detecting statistically significant differences in quantitative MRI experiments, applied to diffusion tensor imaging. *IEEE T MED IMAGING* 34, 1164–1176.
- Price, S., Jena, R., Burnet, N., Hutchinson, P., Dean, A., Pena, A., Pickard, J., Carpenter, T., Gillard, J., 2006. Improved delineation of glioma margins and regions of infiltration with the use of diffusion tensor imaging: an image-guided biopsy study. *American journal of neuroradiology* 27, 1969–1974.
- Pujol, S., Wells, W., Pierpaoli, C., et al, 2015. The DTI challenge: Toward standardized evaluation of diffusion tensor imaging tractography for neurosurgery. *J Neuroimaging* 25, 875–882.
- Ramirez-Manzanares, A., Rivera, M., Vemuri, B.C., Carney, P., 2007. Diffusion basis functions decomposition for estimating white matter intravoxel fiber geometry. *Medical Imaging, IEEE Transactions on* 26, 1091–1102.
- Rokem, A., Yeatman, J.D., Pestilli, F., Kay, K.N., Mezer, A., van der Walt, S., Wandell, B.A., 2015. Evaluating the accuracy of diffusion MRI models in white matter. *PLoS One* 10, e0123272.
- Rose, S.E., Chen, F., Chalk, J.B., Zelaya, F.O., Strugnell, W.E., Benson, M., Semple, J., Doddrell, D.M., 2000. Loss of connectivity in Alzheimer’s disease: an evaluation of white matter tract integrity with colour coded MR diffusion tensor imaging. *Journal of Neurology, Neurosurgery & Psychiatry* 69, 528–530.
- Rueda, S., Fathima, S., Knight, C.L., et al, 2014. Evaluation and comparison of current fetal ultrasound image segmentation methods for biometric measurements: a grand challenge. *IEEE Trans. Med. Im.* 33, 797–813.
- Scherrer, B., Schwartzman, A., Taquet, M., Sahin, M., Prabhu, S.P., Warfield, S.K., 2015. Characterizing brain tissue by assessment of the distribution of anisotropic microstructural environments in diffusion-compartment imaging (DIAMOND). *Magnetic resonance in medicine* .
- Setsompop, K., Kimmlingen, R., Eberlein, E., Witzel, T., Cohen-Adad, J., McNab, J.A., Keil, B., Tisdall, M.D., Hoecht, P., Dietz, P., et al., 2013. Pushing the limits of in vivo diffusion MRI for the Human Connectome project. *NeuroImage* 80, 220–233.
- Sherbondy, A.J., Rowe, M.C., Alexander, D.C., 2010. Microtrack: An algorithm for concurrent projectome and microstructure estimation, in: Jiang, T., Navab, N., Pluim, J., Viergever, M. (Eds.), *Medical Image Computing and Computer-Assisted Intervention MICCAI 2010*. Springer Berlin Heidelberg. volume 6361 of *Lecture Notes in Computer Science*, pp. 183–190. doi:10.1007/978-3-642-15705-9_23.

- Sotiropoulos, S.N., Behrens, T.E., Jbabdi, S., 2012. Ball and rackets: inferring fiber fanning from diffusion-weighted MRI. *NeuroImage* 60, 1412–1425.
- Stanisz, G.J., Wright, G.A., Henkelman, R.M., Szafer, A., 1997. An analytical model of restricted diffusion in bovine optic nerve. *Magnetic Resonance in Medicine* 37, 103–111.
- Stejskal, E.O., Tanner, J.E., 1965. Spin diffusion measurements: Spin echoes in the presence of a time-dependent field gradient. *The Journal of Chemical Physics* 42.
- Tournier, J.D., Calamante, F., Gadian, D.G., Connelly, A., 2004. Direct estimation of the fiber orientation density function from diffusion-weighted MRI data using spherical deconvolution. *Neuroimage* 23, 1176–1185.
- Tuch, D.S., 2004. Q-ball imaging. *Magnetic resonance in medicine* 52, 1358–1372.
- Van Gelderen, P., DesPres, D., van Zijl, P., Moonen, C.T., 1994. Evaluation of restricted diffusion in cylinders. phosphocreatine in rabbit leg muscle. *Journal of Magnetic Resonance Series B* 103, 255–260.
- Vangelder, P., DesPres, D., Vanzijl, P., Moonen, C., 1994. Evaluation of restricted diffusion in cylinders. phosphocreatine in rabbit leg muscle. *Journal of Magnetic Resonance, Series B* 103, 255–260.
- Werring, D., Brassat, D., Droogan, A., Clark, C., Symms, M., Barker, G., MacManus, D., Thompson, A., Miller, D., 2000. The pathogenesis of lesions and normal-appearing white matter changes in multiple sclerosis. *Brain* 123, 1667–1676.
- White, N.S., Leergaard, T.B., D’Arceuil, H., Bjaalie, J.G., Dale, A.M., 2013. Probing tissue microstructure with restriction spectrum imaging: Histological and theoretical validation 34, 327–346.
- Yablonskiy, D.A., Bretthorst, L.G., Ackerman, J.J., 2003. Statistical model for diffusion attenuated MR signal. *Magnetic Resonance in Medicine* 50, 664–669.
- Zhang, H., Schneider, T., Wheeler-Kingshott, C.A., Alexander, D.C., 2012. NODDI: Practical in vivo neurite orientation dispersion and density imaging of the human brain. *NeuroImage* 61, 1000–1016.
- Zou, H., Hastie, T., 2005. Regularization and variable selection via the elastic net. *J. R. Stat. Soc. Series B Stat. Methodol.* 67, 301–320.
- Zou, H., Hastie, T., Tibshirani, R., Others, 2007. On the “degrees of freedom” of the lasso. *Ann. Stat.* 35, 2173–2192.

Acquisition Protocol

	Nr	Δ	TE	G	b		Nr	Δ	TE	G	b
		(ms)	(ms)	(mT/m)	(s/mm ²)			(ms)	(ms)	(mT/m)	(s/mm ²)
$\delta = 3ms$	1	22	49	61	50		25	22	58	58	300
	2	22	49	86	100		26	22	58	95	800
	3	22	49	192	500		27	22	58	190	3,200
	4	22	49	285	1,100		28	22	58	275	6,700
	5	40	67	63	100		29	40	72	59	600
	6	40	67	100	250		30	40	72	100	1,700
	7	40	67	200	1,000		31	40	72	200	6,850
	8	40	67	289	2,100		32	40	72	292	14,550
	9	60	87	63	150		33	60	92	34	300
	10	60	87	103	400		34	60	92	100	2,650
	11	60	87	199	1,500		35	60	92	200	10,500
	12	60	87	290	3,200		36	60	92	292	22,350
	13	80	107	63	200		37	80	112	61	1,300
	14	80	107	99	500		38	80	112	100	3,550
	15	80	107	201	2,050		39	80	112	200	14,150
	16	80	107	291	4,300		40	80	112	292	30,200
	17	100	127	63	250		41	100	132	60	1,600
	18	100	127	101	650		42	100	132	100	4,450
	19	100	127	200	2,550		43	100	132	200	17,850
	20	100	127	291	5,400		44	100	132	292	38,050
	21	120	147	63	300		45	120	152	60	1,950
	22	120	147	99	750		46	120	152	100	5,350
	23	120	147	199	3,050		47	120	152	200	21,500
	24	120	147	291	6,500		48	120	152	292	45,900

Note: We provide signal for the parts of protocol marked in black. In red is the protocol for which the signal needs to be predicted.

Table 1: The scanning protocol used, acquired in ~ 8 hours over two non-stop sessions. The protocol has 48 shells, each with 45 unique gradient directions (‘blip-up-blip-down’).

	Type of model	Nb of free param. (genu/fornix)	Models effect of δ and Δ	Noise assumption	Optimization algorithm	Outliers strategy	Special signal prediction strategy
R-Manzanares	Tissue	–	Yes	Gaussian	weighted-LS bootstrapping	Yes	CV
Nilsson	Tissue	< 12/12	Yes	Gaussian	LM	Yes	CV
Scherrer	Tissue	10/16	No	Gaussian	Bobyqa	Yes	No
Ferizi_1	Tissue	< 12/12	Yes	approx.-Rician	LM	No	No
Ferizi_2	Tissue	< 10/10	Yes	approx.-Rician	LM	No	No
Alipoor	Signal	17/17	No	Gaussian	weighted-LS	Yes	No
Sakaie	Signal	–	No	Gaussian	nonlinear-LS	Yes	No
Rokem	Tissue	< 16,300	No	Gaussian + Noise floor	Elastic net	No	CV
Eufracio	Tissue	7/7	No	Gaussian	bounded-LS Lasso, Ridge	No	No
Loya-Olivas_1	Tissue	11	No	Gaussian	bounded-LS & Lasso	No	No
Loya-Olivas_2	Tissue	5	No	Gaussian	bounded-LS	No	No
Poot	Signal	103	No	Rician	LM-like	No	No
Fick	Signal	475	Yes	Gaussian	Laplacian-reg-LS	No	CV
Rivera	Signal	–	Yes	Gaussian	Weighted Lasso	Yes	CV

Table 2: Summary of the various diffusion models evaluated. Tissue models are models that include an explicit description of the underlying tissue microstructure with a multi-compartment approach. In contrast, signal models focus on describing the DW signal attenuation without explicitly describing the underlying tissue and rather correspond to a “signal processing” approach. (Abbreviations: LS=Least Squares, LM=Levenberg-Marquardt, CV=cross-validation, reg=regularized.)

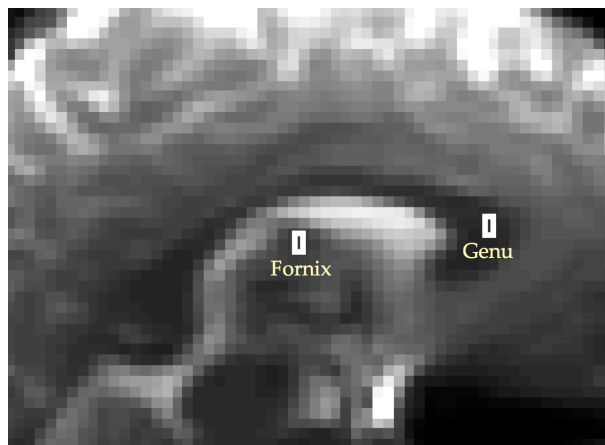


Figure 1: We only consider two ROIs, each containing six voxels from the genu in the corpus callosum, where the fibres are approximately straight and parallel, and from the fornix, where the configuration of fibres is more complex.

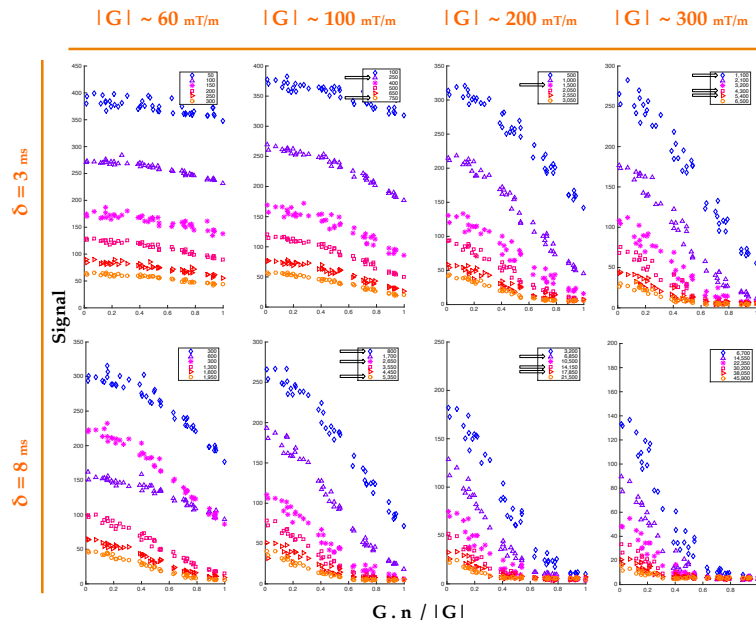


Figure 2: Diffusion weighted signal from the genu ROI, averaged over the six voxels. Across each column and row, the signal pertains to one of the gradient strengths or pulse times δ used; while in each subplot, the six shells shown in different colours are Δ -specific, increasing in value (22, 40, 60, 80, 100, 120 ms) from top to bottom. Inside the legend, the b-value is in s/mm^2 units; here, the HARDI shells kept for testing are those marked with a horizontal arrow; the remaining shells comprise training data. On the x-axis is the cosine of the angle between the applied diffusion gradient vector \mathbf{G} and the fibre direction \mathbf{n} .

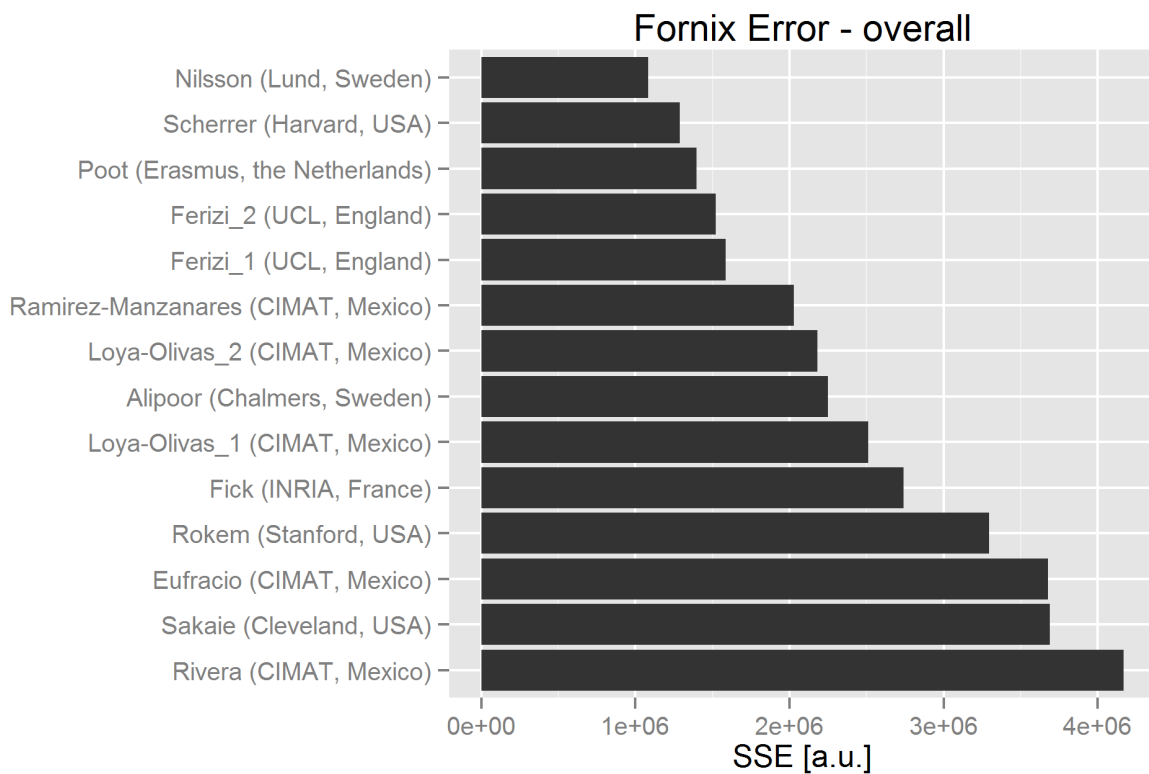
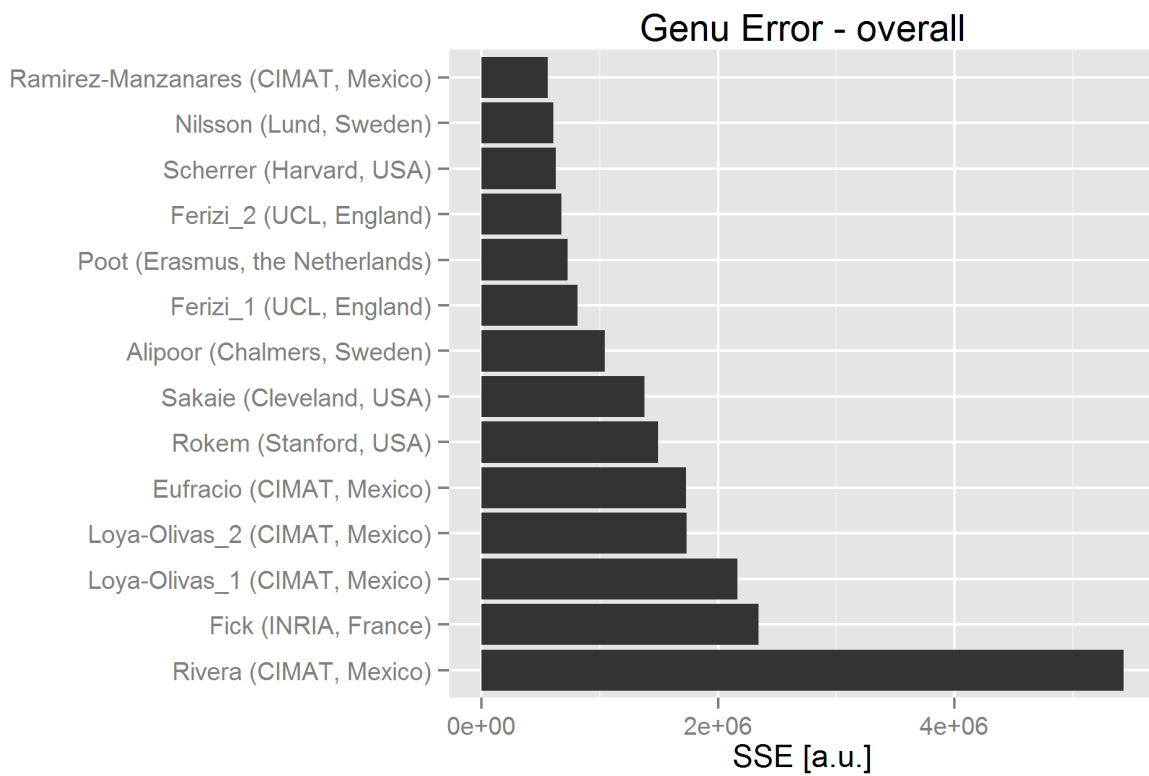


Figure 3: Overall ranking of models by sum-of-squared-error metric over all voxels in genu (top) and fornix (bottom) ROIs.

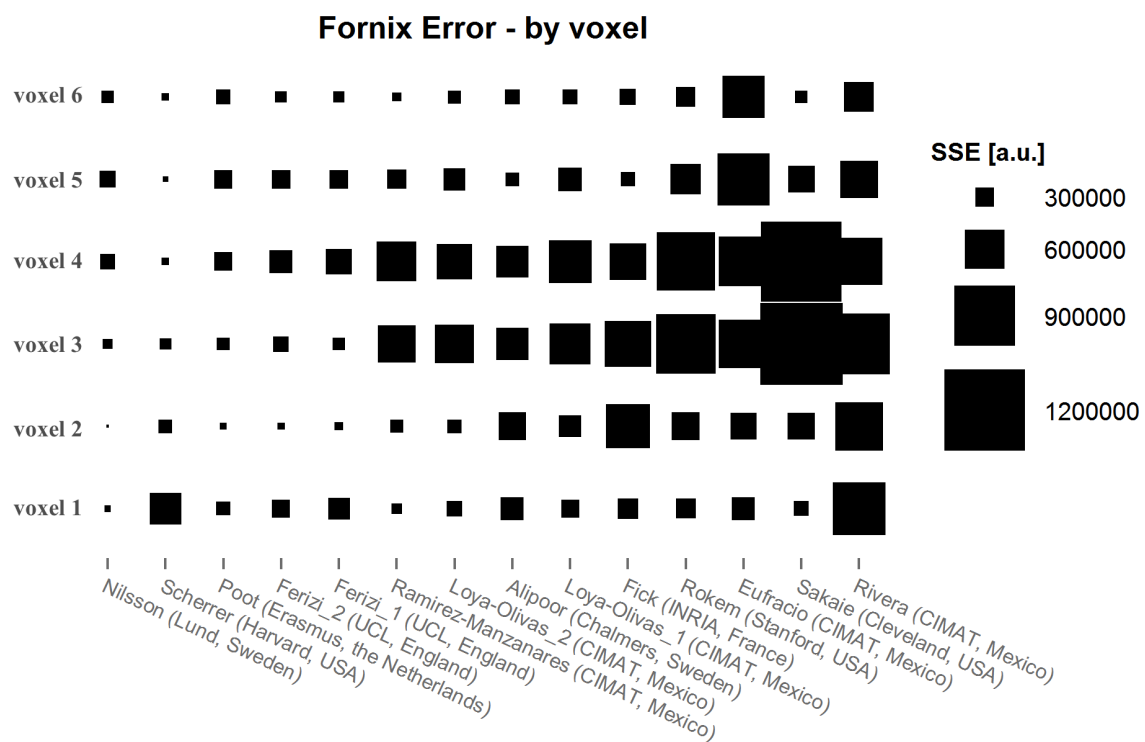
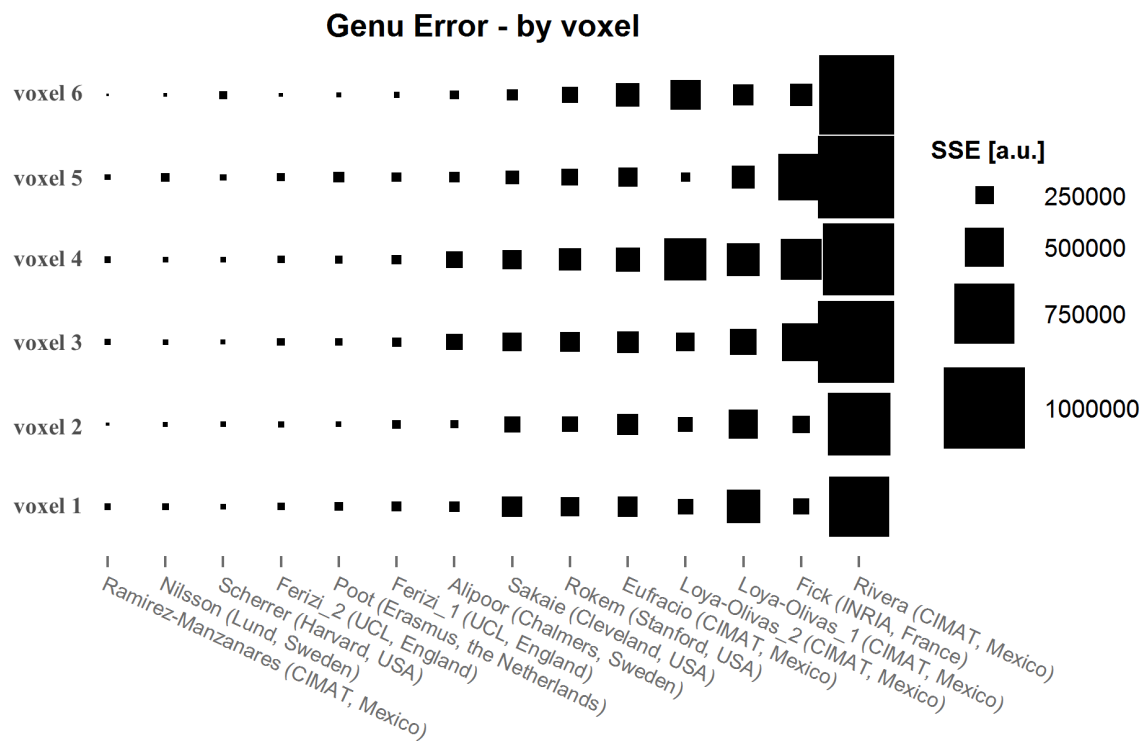


Figure 4: Sum-of-squared-error per voxel for each model in genu and fornix. The size of rectangles represent the SSE value per voxel.

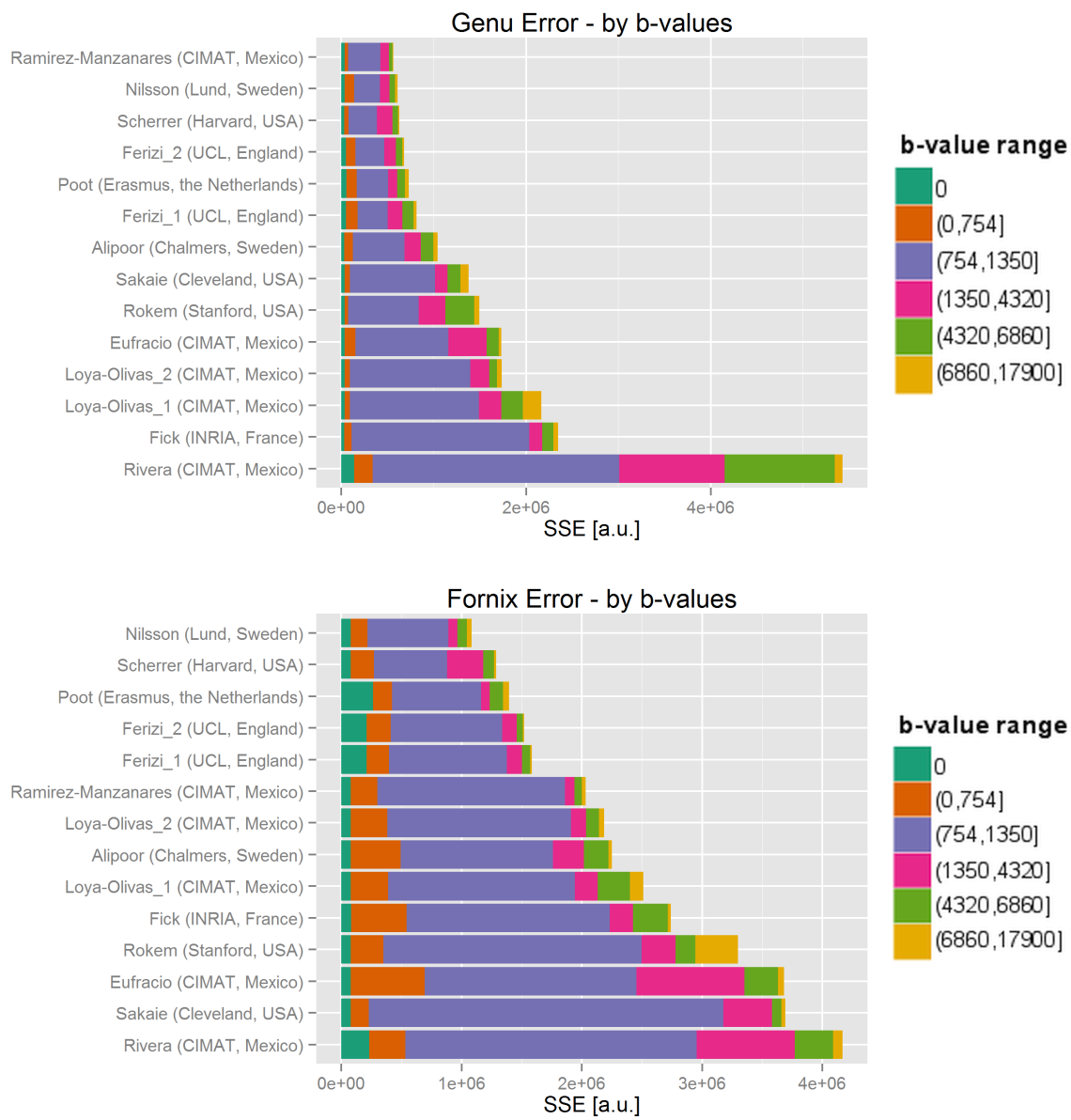


Figure 5: Sum-of-squared-error for each model in all voxels in genu and fornix ROIs. The colors represent different ranges of b-value shells.

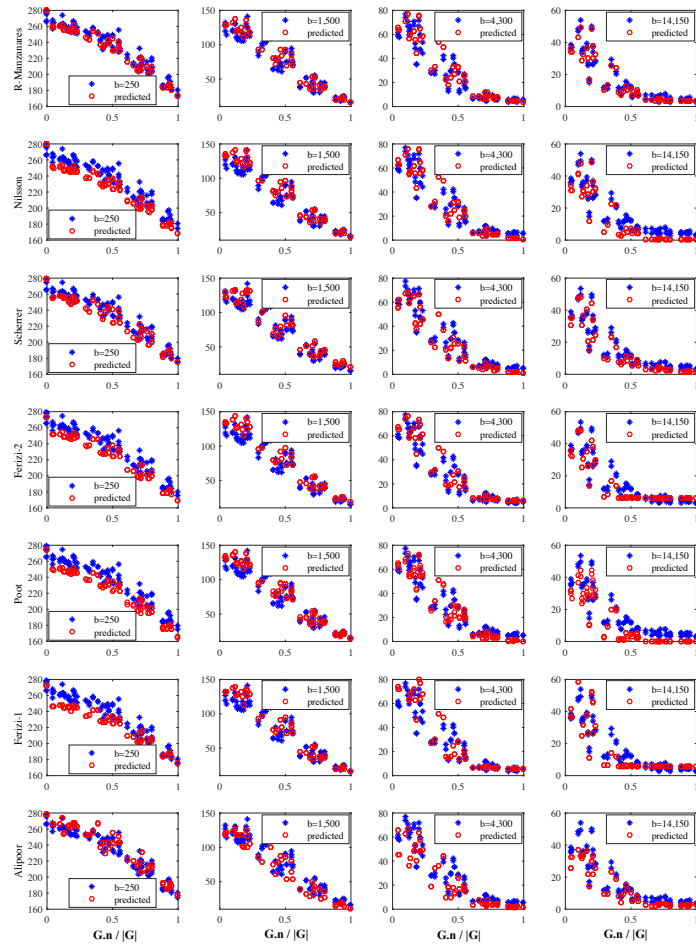


Figure 6: An illustration of the observed and predicted genu signal of 7 of the 14 best models, shown in red circles, to 4 (of the total 12) representative shells, shown in blue stars. The best models are listed first. The axes are as in Fig.2.

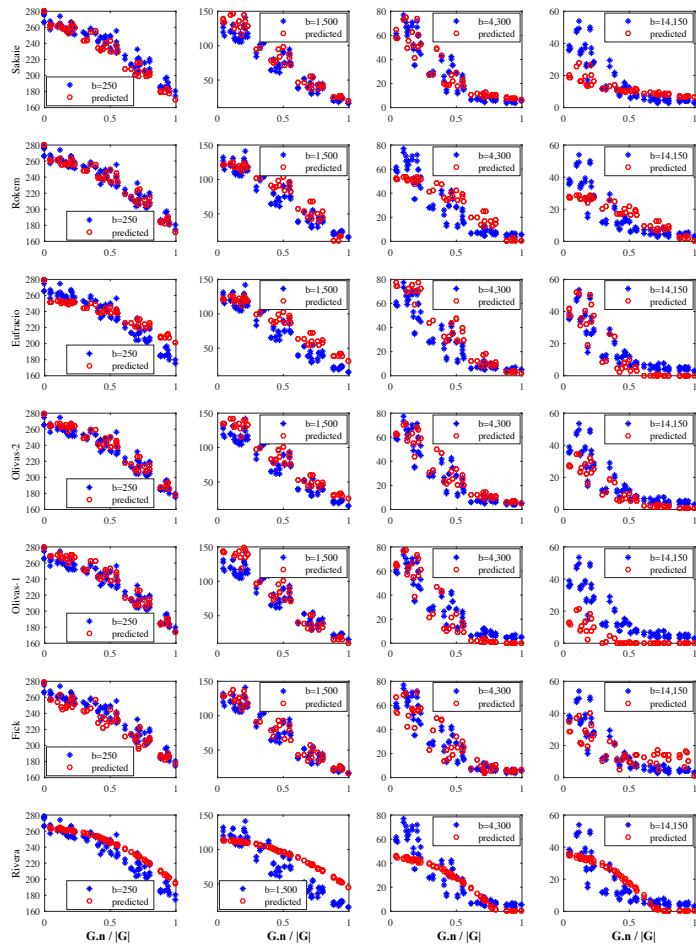


Figure 7: Similar to Fig.6, here we show the remaining 7 model synthesized signals.